The Relationship between Equatorial Mixed Rossby–Gravity and Eastward Inertio-Gravity Waves. Part II

JULIANA DIAS

CIRES, University of Colorado, and NOAA/Earth System Research Laboratory, Boulder, Colorado

GEORGE N. KILADIS

Physical Sciences Division, NOAA/Earth System Research Laboratory, Boulder, Colorado

(Manuscript received 7 August 2015, in final form 16 February 2016)

ABSTRACT

Space–time spectral analysis of tropical cloudiness data shows strong evidence that convectively coupled $n = 0$ mixed Rossby–gravity waves (MRGs) and eastward inertio-gravity waves (EIGs) occur primarily within the western/central Pacific Ocean. Spectral filtering also shows that MRG and EIG cloudiness patterns are antisymmetric with respect to the equator, and they propagate coherently toward the west and east, respectively, with periods between 3 and 5 days, in agreement with Matsuno's linear shallow-water theory. In contrast to the spectral approach, in a companion paper it has been shown that empirical orthogonal functions (EOFs) of 2–6-day-filtered cloudiness data within the tropical Pacific Ocean also suggest an antisymmetric pattern, but with the leading EOFs implying a zonally standing but poleward-propagating oscillation, along with the associated tropospheric flow moving to the west. In the present paper, these two views are reconciled by applying an independent approach based on a tracking method to assess tropical convection organization. It is shown that, on average, two-thirds of MRG and EIG events develop independently of one another, and one-third of the events overlap in space and time. This analysis also verifies that MRG and EIG cloudiness fields tend to propagate meridionally away from the equator. It is demonstrated that the lack of zonal propagation implied from the EOF analysis is likely due to the interference between eastward- and westward-propagating disturbances. In addition, it is shown that the westward-propagating circulation associated with the leading EOF is consistent with the expected theoretical behavior of an interference between MRGs and EIGs.

1. Introduction

In a companion paper (Kiladis et al. 2016, hereafter K16), evidence was presented of a zonally standing mode in antisymmetric convection about the equator related to the $n = 0$ mixed Rossby–gravity wave (MRG) and eastward inertio-gravity wave (EIG) continuum from the equatorial shallow-water theory of Matsuno (1966). As discussed in K16, while MRGs have been studied extensively over the last half century in both the troposphere and the stratosphere, individual cases of EIGs are much more elusive, even though their spectral signals are quite strong. K16 also show that MRG circulations in the lower stratosphere are observed at all longitudes along the equator, while eddies centered on the equator-associated tropospheric MRGs are detectable over all ocean basins, but their strengths and time scales vary with height. Moreover, MRGs coupled to convection appear to be much more geographically constrained to the west-central Pacific, with much weaker coupling over the Atlantic and Indian Ocean sectors. This confirms earlier work by Liebmann and Hendon (1990), Hendon and Liebmann (1991), and Dias and Kiladis (2014). Similarly, there is also an indication that convectively coupled EIGs are strongest within the western/central Pacific, with a much weaker secondary peak in activity over the Indian Ocean sector (Dias and Kiladis 2014; K16).

Observational studies based on spectral filtering show that MRG and EIG cloudiness perturbation patterns are consistent with Matsuno's theory in that they are antisymmetric with respect to the equator and they propagate coherently with the tropospheric flow toward the west and east, respectively. The period is, on average,

Corresponding author address: Juliana Dias, Physical Sciences Division, NOAA/ESRL, R/PSD1, 325 Broadway, Boulder, CO 80305.
E-mail: juliana.dias@noaa.gov

DOI: 10.1175/JAS-D-15-0231.1

close to 4.5 days for convectively coupled MRGs is and is around 3 days for EIGs (Wheeler and Kiladis 1999; Wheeler et al. 2000; Kiladis et al. 2009). Their combined signals produce very strong peaks in the 3–6-day range in raw spectra (Yanai et al. 1968; Wallace and Chang 1969; K16). The results in K16 are based on a coherence analysis of circulation and Cloud Archive User System (CLAUS) tropical brightness temperature (T_b) data, along with an empirical orthogonal function (EOF) decomposition of the same data using a 2–6-day bandpass-filtered T_{b26}. A striking result from K16 is that the first two T_{b26} EOFs are also antisymmetric with respect to the equator but are dominated by poleward propagation with a 3–5-day period, despite the fact that their circulations are associated with westward-propagating MRG-like eddies centered on the equator expected from Matsuno's theory. This implies that the propagation characteristics of the leading modes of synoptic convective variability in the Pacific inferred from the EOF versus spectral analysis are not completely in agreement with one another. The main objective of this paper is to reconcile these two views. To this end, we will extend the analysis from K16 in order to clarify whether the zonally standing pattern of oscillation in the western/central Pacific corresponds to a real physical phenomenon or if it is an artifact of the EOF analysis caused, for instance, by an interference signal between westward- and eastward-propagating 3–5-day disturbances.

Theories for MRG initiation in the troposphere range from lateral forcing (Mak 1969; Lamb 1973; Hayashi 1976; Wilson and Mak 1984), to nonlinear wave–convective instability of the second kind (Itoh and Ghil 1988), nonlinear resonance (Raupp and Silva Dias 2005), evaporation–wind feedback (Goswami and Goswami 1991), or meridional and vertical shear instabilities (Zhang and Webster 1989; Wang and Xie 1996; Xie and Wang 1996; Han and Khouider 2010; Zhou and Kang 2013). One particular issue that is unresolved concerns the reason that convectively coupled MRGs and EIGs are constrained to a relatively narrow longitudinal sector. Observational studies such as Zangvil and Yanai (1980), Yanai and Lu (1983), Magaña and Yanai (1995), and K16 find strong links between lateral forcing and MRGs, although such forcing is not confined to the western/central Pacific sector. Similarly, Goswami and Goswami (1991) show that both MRG and EIG instabilities only occur in their shallow-water framework when surface basic-state winds are easterlies, which is also not a feature exclusive to the western/central Pacific sector. Both Itoh and Ghil (1988) and Raupp and Silva Dias (2005) offer some compelling arguments for the geographic selection of MRG and EIG modes; however, to the authors' knowledge, there has been no observational support for their theories. In summary, it appears that theories concerning the dynamics of MRGs and EIGs would benefit from a more complete observational assessment of the behavior of these types of disturbances.

There is ample evidence of local and remote impacts of organized subseasonal tropical rainfall (Frank and Roundy 2006; Gloeckler and Roundy 2013; Schreck et al. 2011); however, most of the current climate models poorly resolve this type of variability, and convectively coupled MRGs and EIGs are no exception. For instance, Hung et al. (2013) show that most models from phase 5 of the Coupled Model Intercomparison Project (CMIP5) do not reproduce the observed strong MRG concentration over the western/central Pacific. In addition, CMIP5 precipitation space–time power spectra along the MRG and EIG dispersion curve vary widely in comparison with observations, from a complete lack of MRG and EIG power, to having too strong of an MRG signal, or to showing only a large wavenumber-0 spectral peak. Model physical parameterizations are likely to be a major source of these differences. In particular, both the type and tuning of cumulus parameterizations, which are key to the physical processes involved in the coupling between convection and the larger-scale flow, have been shown to strongly affect a model's ability to resolve convectively coupled equatorial waves (CCEWs) and other tropical disturbances (Lin et al. 2008; Straub et al. 2010; Frierson et al. 2011). The difficulties in modeling convectively coupled MRGs and EIGs are perhaps not surprising given the large number of disparate ideas put forth to account for their initiation and maintenance. Observational understanding of the nature of the coupling between MRG and EIG dynamics and rainfall is, therefore, an important step toward improving the ability of models to predict and simulate synoptic-scale variability in the tropics.

Here we investigate whether the observed MRG and EIG convective variability in the western/central Pacific is mainly due to a (i) zonally standing oscillation, (ii) interference between westward and eastward wavelike disturbances, or (iii) westward and eastward wavelike disturbances that alternate in time. By interference in (ii), we include both possibilities of preexisting westward and eastward disturbances propagating toward one another and continuing to propagate toward the west and east, respectively, and also cases where westward and eastward disturbances initiate simultaneously because of external forcing. Using the same datasets as in K16, namely CLAUS T_b and ERA-Interim (ERAI), we will show that there is evidence for all of these possibilities in the data, and they are all consistent with

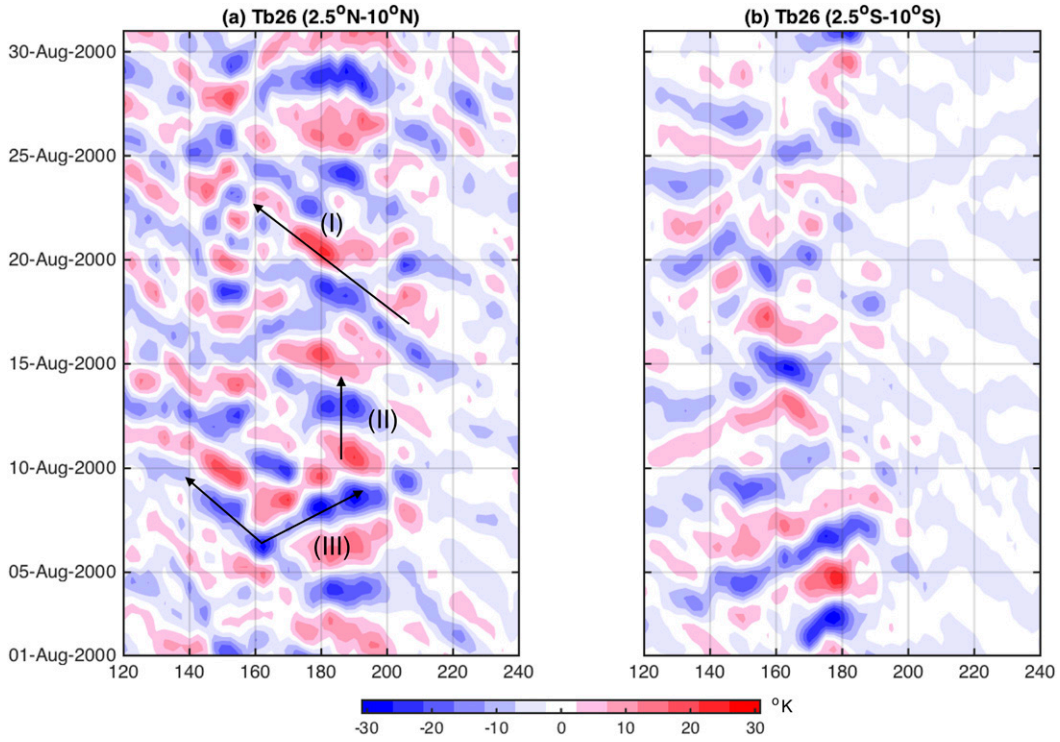

FIG. 1. Time–longitude section of 2–6-day-filtered CLAUS T_{b26} in the tropical Pacific averaged (a) from 2.5° to 10°N and (b) from 2.5° to 10°S. Labels represent examples of a westward disturbance (I), a standing oscillation (II), and eastward and westward disturbances in the same location (III).

Matsuno's shallow-water theory. These three possible interpretations of the EOF pattern from K16 are illustrated in the time–longitude section of T_{b26} shown in Fig. 1a, which shows an initial period where there are westward and eastward disturbances simultaneously near the date line, followed by a period where there is a standing oscillation in the same region and then a period of mostly westward-propagating disturbances. Comparison between Figs. 1a and 1b reveals that these disturbances are often, but not always, antisymmetric with respect to the equator. This asymmetry will be discussed in detail later.

The paper outline is as follows. In section 2, we review MRG and EIG theory, and in section 3 we present an EOF analysis of MRG and EIG theoretical shallow-water modes. This analysis serves two purposes. First, by using an input dataset containing a known signal, we can test the ability of EOFs to distinguish between the types of wave patterns described above in points (i), (ii), and (iii). Second, it gives us insight into what we should expect from the T_{b26} EOF analysis if convectively coupled MRGs and EIGs were the dominant modes. In section 4, we undertake an independent approach to assess synoptic convective organization that does not rely on either an EOF decomposition or a 2–6-day bandpass filter. This technique allows us to detect times consistent with (i), (ii), and (iii). A summary and conclusions are presented in section 5.

2. Review of MRG and EIG dynamics

MRGs and EIGs are normal modes of the linear shallow-water equations (Matsuno 1966):

$$\frac{\partial u}{\partial t} - \beta y v + \frac{\partial \phi}{\partial x} = 0,$$
$$\frac{\partial v}{\partial t} + \beta y u + \frac{\partial \phi}{\partial y} = 0, \quad \text{and}$$
$$\frac{\partial \phi}{\partial t} + c^2 \nabla_H \cdot \mathbf{v} = 0, \tag{1}$$

where the variables are the horizontal velocity u and v and the geopotential ϕ. The parameters are the gravity wave speed $c = \sqrt{gH_{\text{eq}}}$, the equivalent depth H_{eq}, and $\beta = 2\Omega/R$, where Ω and R are Earth's angular velocity and radius, respectively. In the next section, we use $H_{\text{eq}} = 25$ m for the convectively coupled modes since that appears to best fit the data (Wheeler and Kiladis 1999; Kiladis et al. 2009; K16, their Fig. 1a). The normal modes are obtained by the method of separation of variables, which yields the dispersion relation:

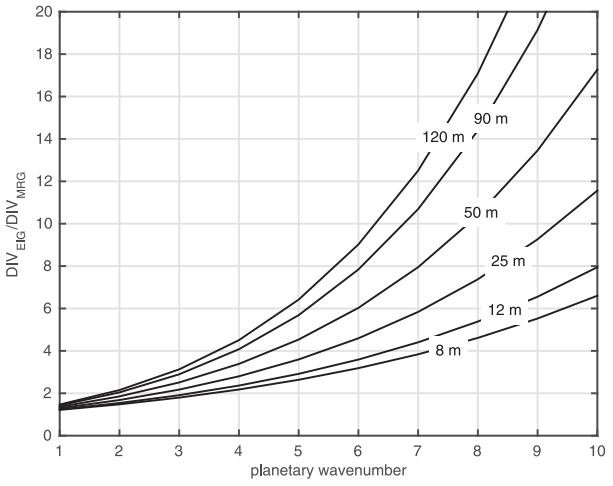

FIG. 2. Ratio of EIG to MRG divergence [from (6)] as a function of zonal wavenumber for H_{eq} = 8, 12, 25, 50, 90, and 120 m.

$$\frac{\omega^2}{c^2} - k^2 - \frac{k}{\omega}\beta = \frac{\beta}{c}(2n+1), \tag{2}$$

where ω is the frequency, k is the zonal wavenumber, and the parameter n is related to the meridional structure of each mode (Matsuno 1966). The MRG and EIG modes correspond to the case where $n = 0$. In this case, the MRG and EIG frequencies are, respectively, the negative and positive roots of (2):

$$\omega_{\pm} = \frac{ck}{2} \pm \sqrt{\frac{c^2k^2}{4} + c\beta}. \tag{3}$$

As discussed in K16 (section 2), an interesting contrast between MRG and EIG dynamics is related to their divergence fields. This contrasting behavior can be directly inferred based on their analytical divergence:

$$\text{div} = -\frac{y}{c}(\omega_{\pm}k + \beta)\cos(kx - \omega_{\pm}t)e^{-\beta y^2/2c}, \tag{4}$$

where the term $\omega_{\pm}k$ comes from the zonal gradient and β comes from the meridional gradient. In the case of MRGs, zonal convergence is out of phase with meridional convergence. In contrast, zonal and meridional convergences are in phase in the case of EIG. Based on the dispersion relation, MRGs and EIGs also satisfy

$$\omega_{\pm}k + \beta = \frac{\omega_{\pm}^2}{c} > 0. \tag{5}$$

Note that (4) and (5) imply that

$$\left|\frac{\text{div}_{\text{EIG}}}{\text{div}_{\text{MRG}}}\right| = \left(\frac{\omega_+}{\omega_-}\right)^2 > 1. \tag{6}$$

Figure 2 shows the ratio in (6) as a function of zonal wavenumber for several values of H_{eq} and implies that, given the same external forcing, the total circulation of the MRG response is much stronger than that for EIGs, particularly for deeper H_{eq}. However, even for the observed scales of convectively coupled MRGs and EIGs ($H_{eq} \approx 25$ m), Fig. 2 shows that the MRG velocity field has to be 4 times larger than that of the EIG in order for both disturbances to have the same divergence amplitude (Fig. 3 in K16). In the stratosphere where $H_{eq} \approx 120$ m, this ratio is even larger and could explain the large westward bias in spectral power seen in Fig. 1b from K16 as well as the fact that the leading EOFs of zonal wind at 50 hPa (see Fig. 4 in K16) reveal only westward-moving modes. We discuss these issues further in section 4.

3. EOF analysis

a. Idealized data

In this section, we use two idealized cases to test the ability of EOFs to distinguish between various types of interference signals discussed in the introduction. First, we superimpose the theoretical dynamical fields associated with a single MRG and EIG mode, where all fields are normalized to the same maximum divergence amplitude, and they are in phase at the initial time (as in Fig. 3 of K16). We choose the divergence field because horizontal low-level convergence is proportional to ascent in a baroclinic model; thus, it is used here as a proxy for moist convection. The second idealized case is similar, except that for half the time the dataset is made up of only MRG modes, followed by only EIG modes. Time–longitude samples of these divergence fields are shown in Fig. 3. The first case shown on the left panel is denoted "MRG+EIG" and the second shown on the right is denoted "MRG/EIG." In both cases, the first two EOFs are in quadrature and represent propagating patterns similar to the MRG and EIG divergence seen in Fig. 2 in K16, together explaining about 99% of the total variance. As an aside, it is shown in appendix A that the amount of variance explained by the first two EOFs is substantially decreased by adding small-amplitude noise to either MRG+EIG or MRG/EIG data, suggesting that, despite the relatively small variance explained, the first two EOFs of observed T_{b26} in K16 are consistent with physical processes.

Since the normalization implies that $v_{\text{MRG}} > v_{\text{EIG}}$, the regression of meridional winds onto the first principal component (PC) of the idealized MRG+EIG (Fig. 4) shows westward propagation similar to the analogous analysis based on the leading PC of T_{b26} (see K16, their

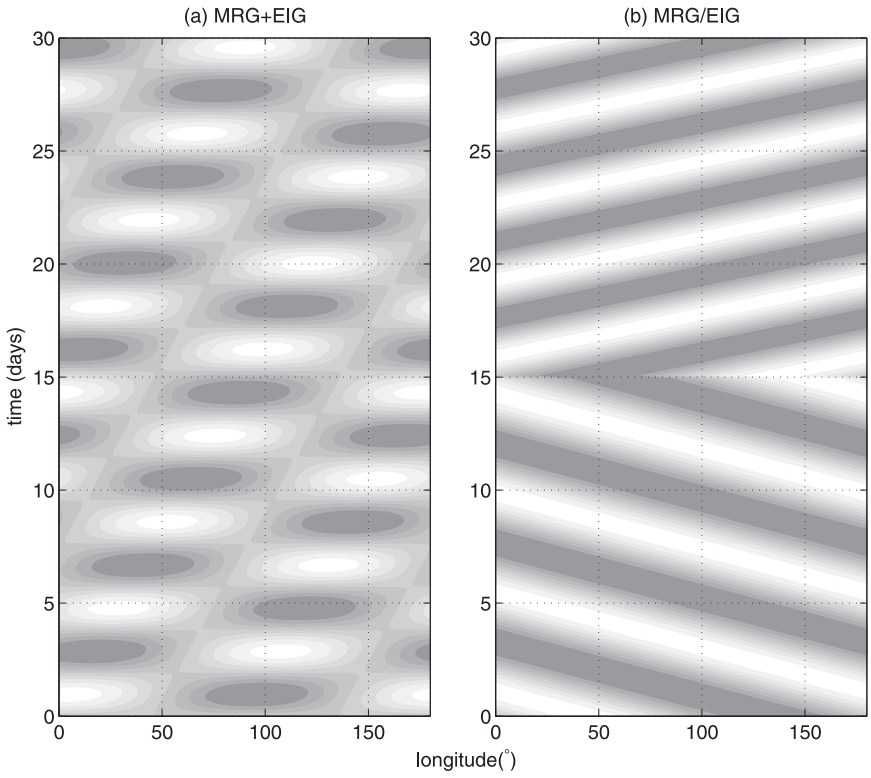

FIG. 3. Time–longitude diagram of (a) MRG+EIG and (b) MRG/EIG nondimensional divergence fields at 7.5°N (see details in the text). The wave parameters used are $k = 2$ and $H_{eq} = 25$ m. Dark (light) gray shading is for positive (negative) anomalies.

Fig. 7). A similar result is obtained using the idealized MRG/EIG PCs (not shown). On the other hand, the divergence regressed onto either MRG+EIG or MRG/EIG suggests slow eastward propagation, because for a fixed wavenumber the EIG phase speed is larger than that of the MRG. In fact, by adjusting H_{eq} of either MRG or EIG modes so that the amplitude of their phase speeds match, an analogous EOF decomposition yields westward-propagating regressed meridional winds and a standing pattern in the divergence (not shown). A similar result is obtained by adding a Kelvin wave mode to MRG+EIG or MRG/EIG (not shown), which is likely what occurs at times in T_{b26} data, because the 2–6-day band overlaps with variability associated with convectively coupled Kelvin waves (Wheeler and Kiladis 1999; Kiladis et al. 2009).

While the EOF patterns are very similar in both MRG+EIG and MRG/EIG cases, their differences can be readily captured by lag correlating the first two PCs. Specifically, the lag correlation between the first two PCs in both MRG+EIG and MRG/EIG cases are in very close agreement, including the overall weak lag correlation (solid black and dashed black lines in Fig. 5); however, computing the lag correlation during the MRG period only (solid gray line in Fig. 5) or EIG only (dashed gray line in Fig. 5) reveals much stronger correlations at the expected lags, given the prescribed MRG and EIG periods. To summarize, the EOF analysis applied to idealized cases suggests that weak lag correlation between the first two PCs of T_{b26} does not necessarily imply that the first two EOFs are independent or that one of them represents a standing oscillation pattern. That is, either interference or alternating westward- and eastward-propagating disturbances can yield such weak correlations between PCs that explain a similar amount of variance, as well as the apparent disagreement between propagation directions of the meridional winds versus divergence. Thus, EOFs applied to theoretical flows suggest that a lag-correlation analysis using a running window based on the leading PCs of T_{b26} could potentially highlight periods where one mode is dominant over the other, and we now turn to this approach.

b. Observations

Using the EOF decomposition from K16, Fig. 6 shows that the lag correlation between the first two T_{b26} PCs (denoted PC1 and PC2) is weak at all lags, with irregular

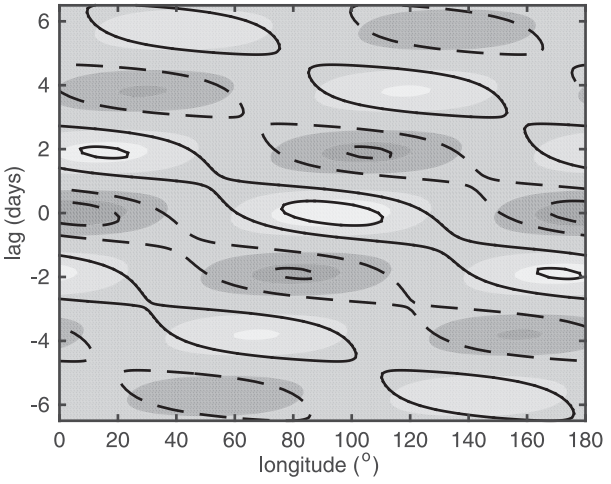

FIG. 4. Lag–longitude diagram of MRG+EIG divergence at 7.5°N (shading) and meridional wind on the equator regressed onto the first PC of MRG+EIG. Both variables are nondimensional, and contour intervals are 1 std dev starting at 1 std dev. Dark gray shading (solid contours) is for positive anomalies and light gray shading (dashed contours) is for negative anomalies.

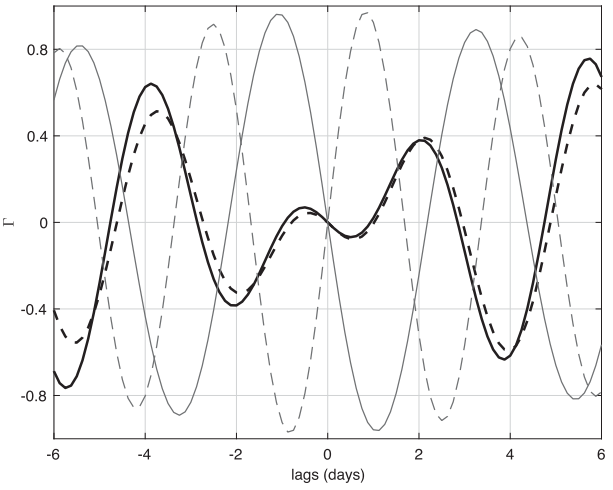

FIG. 5. Lag correlation between the first two PCs of MRG+EIG (solid black), MRG/EIG (dashed black), MRG only (solid gray), and EIG only (dashed gray).

peaks that suggest a nearly 5-day period. Meanwhile, in the case of T_{b26} filtered for westward wavenumbers only T^w_{b26} associated with the pattern in Fig. 8a of K16, correlations are strongest at lags of ±1 days, with correlations at longer lags displaying a 4.25-day period. As mentioned earlier, the hypothesis that naturally emerges is that if T_{b26} is dominated by alternating westward and eastward disturbances (MRG/EIG), we should be able to identify a significant number of alternating periods of strong positive or negative lag-1 correlations. To test this, we calculate time-windowed lag-regression coefficients between PC1 and PC2 of T_{b26}. The time-windowed lag correlation is defined as

$$\Gamma^{N_T}(n,\tau) = \gamma_\tau(\mathrm{pc}_1^n, \mathrm{pc}_2^n), \tag{7}$$

where

$$\mathrm{pc}_i^n = \mathrm{PC}_i(n{:}\, n + N_T - 1), \tag{8}$$

γ_τ is the cross correlation at lag τ, N_T is the discrete time window, and $n = \{1, N_T, 2N_T, \ldots\}$ is such that intervals do not overlap. Both n and N_T are integers corresponding to the number of time steps, and τ units are days. The set of independent time intervals $I_n^{N_T} = \{n{:}\, n + N_T - 1\}$ is not unique in the sense that it depends on the initial date that the index $n = 1$ represents. To address this issue, the following results are an average over various sets $\{I_n^{N_T}\}$, where we vary the initial date from 1 to $N_T - 1$, with the index 1 representing the first record date. We define the dimensional time window: TW $= N_T dt$, where dt is the data time step (3 h).

The choice of TW is motivated by the decorrelation time of PC1 and PC2 using the entire record, which is about 5 days. A short time window of 5 days can be useful in detecting a specific event, whereas a longer time window can capture a period where a particular type of disturbance is dominant; thus, for the following analysis, a range of TWs are used and interpreted accordingly. To physically interpret the time-windowed analysis, recall that based on the EOF patterns shown in K16, positive (negative) correlation at negative lags represents westward (eastward) propagation (see their Fig. 5). The correlation statistical significance is tested based on the p value calculated by transforming the correlation at each lag to create a t statistic with $N_T - 2$ degrees of freedom, and, in the results shown next, we

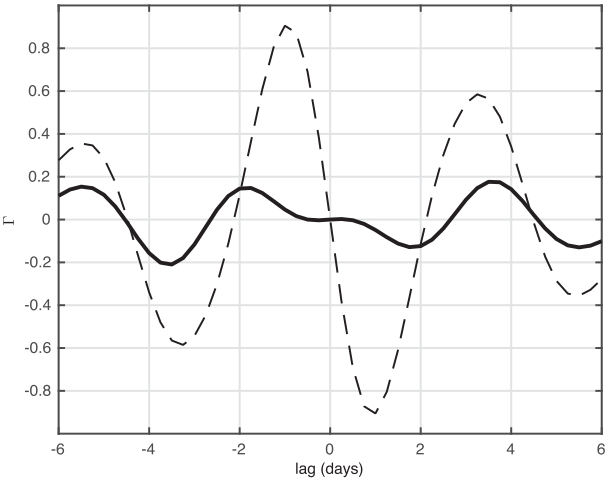

FIG. 6. As in Fig. 5, but for lag correlation between the first two PCs of T_{b26} (solid) and T^w_{b26} (dashed).

use $p < 0.1$ as the threshold for the statistical significance. Other methods based on bootstrapping were tested and yielded similar results (not shown).

In view of the fact that the lag correlation of T_{b26}^{w} peaks at around ±1 day (Fig. 6), our index for selecting westward versus eastward times is based on the mean correlation over lags between −2 and 0 days:

$$\Gamma_{0-2}^{N_T}(n) = \text{mean}[\Gamma^{N_T}(n,\tau)]_{(-2<\tau<0)}. \quad (9)$$

The estimated probability density function (pdf) of statistically significant $\Gamma_{0-2}^{N_T}$ is shown in Fig. 7a for various time windows. The pdfs are clearly bimodal, and for a fixed TW the positive and negative peaks are located at approximately the same correlation amplitude. In addition, there is an inverse relationship between TW and peak correlation amplitude: the larger the TW, the weaker the peak correlation amplitude. Figure 7b shows that the partition between westward- ($\Gamma_{0-2}^{N_T} > 0$) and eastward- ($\Gamma_{0-2}^{N_T} < 0$) propagating segments is close to even, with slightly more westward segments for all choices of TW. The lag-correlation composite on the westward cases (Fig. 7c) is similar to the lag regression of T_{b26}^{w} PC1 and PC2 shown in Fig. 6, whereas the lag-correlation composite on the eastward cases suggests a slightly shorter period, which is consistent with the difference in periods between observed convectively coupled MRGs and EIGs (Wheeler et al. 2000; Kiladis et al. 2009).

It is important to note that, based on our correlation criteria, the propagating segments for all choices of TW represent only about 30% of the total time intervals (Fig. 7b). A similar composite to the ones shown in Fig. 7c, including only the remaining 70% of the cases (i.e., noncorrelated intervals) reveals only weak correlations at all lags, with a very similar structure as the one shown in Fig. 6 (not shown). This result suggests that, while periods of MRG/EIG are present for about 30% of the record in observations, for the remaining 70% we cannot conclude whether the weak correlation between PC1 and PC2 is due to independent standing oscillations or a simultaneous interference between westward and eastward disturbances (MRG+EIG). To resolve this issue, many variations of this method have been attempted, but these produce similarly inconclusive results, which motivated the completely independent analysis presented next.

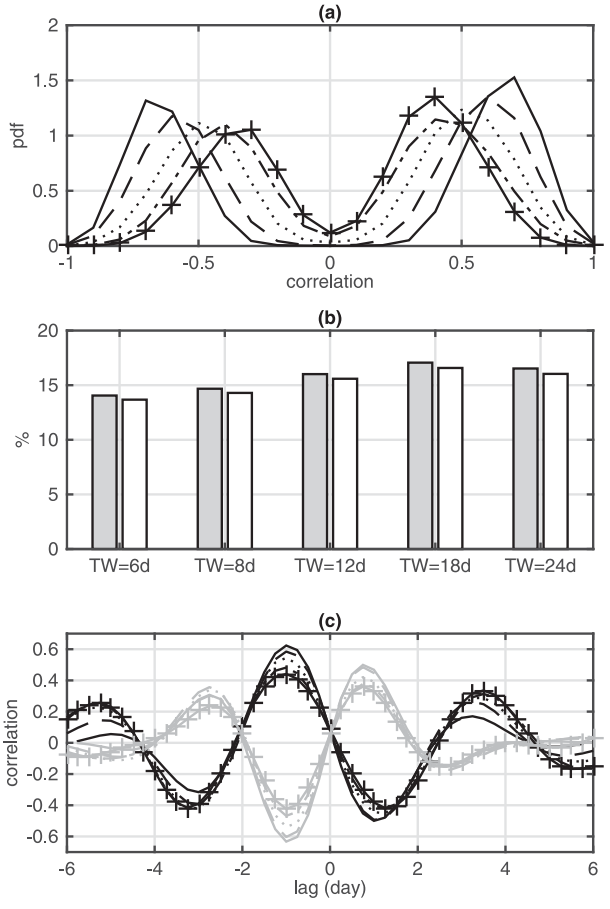

FIG. 7. (a) PDF of $T_{b26}\Gamma_{0-2}^{n}$ using various segment lengths (days): TW = 6 (solid), 8 (dashed), 12 (dotted), 16 (dashed–dotted), and 24 (crosses). (b) Percentage of segments where PCs suggest westward (positive correlation; gray bars) and eastward (negative correlation; white bars) propagation. (c) Lag-correlation composites on westward (black) and eastward segments (gray), where the symbols correspond to different TW following the same convention from (a).

4. An object analysis of MRGs and EIGs

An alternative approach to investigating synoptic convective organization is to objectively identify contiguous cloud regions (CCRs) in T_b data. For object tracking, it is important to use the highest spatial and temporal resolution data possible, so we start with the original 3-hourly T_b dataset at 0.5° horizontal resolution. The algorithm used is presented in detail in Dias et al. (2012); the only difference here is that, instead of applying the detection algorithm to raw T_b data, we apply it to T_b filtered for planetary zonal wavenumbers less than 10 (T_b^{10}). The primary reason to use spatially filtered data is that propagating CCRs in raw data tend to be at mesoscales, whereas synoptic-scale convection is typically as a result of organization of these smaller-scale CCRs (Dias et al. 2012). We choose to filter only in space because we are interested in detecting the life cycle of these synoptic CCRs without preselecting frequencies by using a temporal filter. The wavenumber filter implies that, here, CCRs should be interpreted

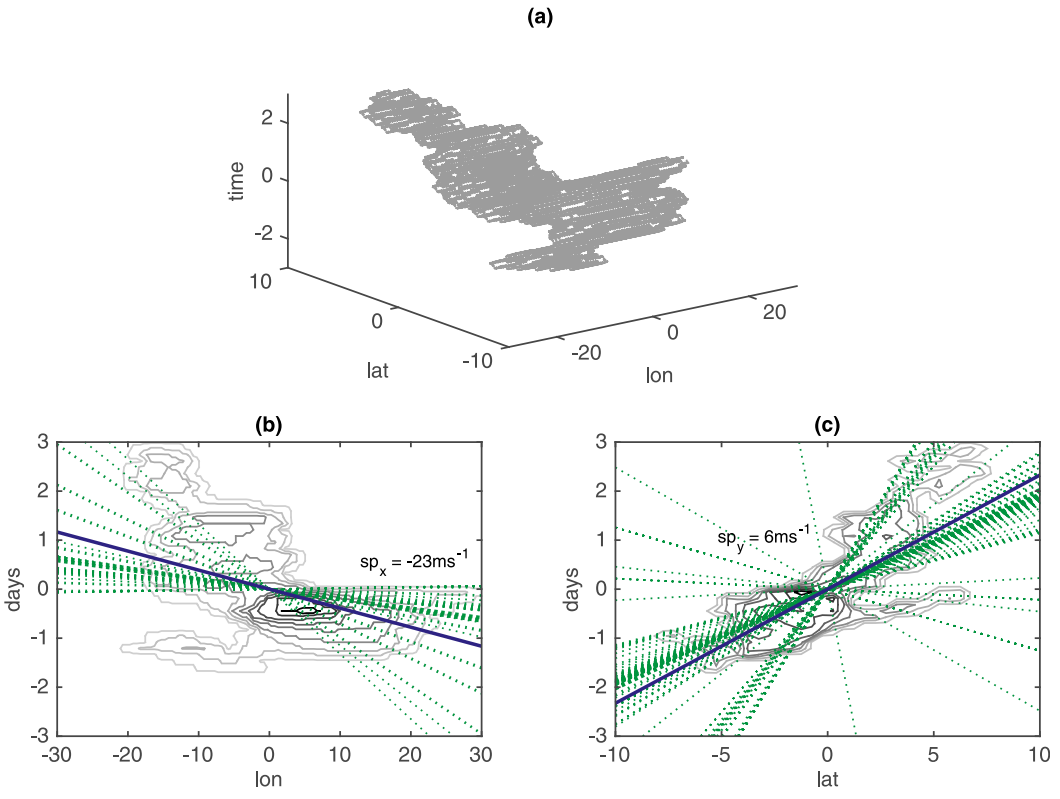

FIG. 8. Example of a coherent CCR: gray contours correspond to (a) longitude–latitude–time view, (b) longitude–time view, and (c) latitude–time view. In (b) and (c) the blue lines show sp_x and sp_y, and the green lines show examples of sp_x^r and sp_y^r (see appendix B for details).

as a proxy for synoptic-scale envelopes of organized convection.

a. Method

While we refer to Dias et al. (2012) for details on the algorithm implementation, it is worthwhile to summarize some of its relevant features. The first step is to search for contiguous regions in the three-dimensional space of latitude, longitude, and time where T_b^{10} falls below a given threshold. To illustrate, Fig. 8a shows one example of a CCR detected in T_b^{10}. The location of each CCR is defined by its centroid in the space of latitude L_y, longitude L_x, and time L_t. Their propagation direction and speed are calculated using the best-fit method developed in Dias et al. (2012) such that, for each CCR, the zonal and meridional speed of propagation (sp_x and sp_y) are estimated. In addition, we develop a test for the coherence of the zonal and meridional CCR propagation characteristics (T_x and T_y), which yields one if the CCR propagates coherently at the estimated speed and zero otherwise. In essence, for each CCR, we test for the sp_x (sp_y) variance across its latitudinal (longitudinal) cross sections (see details in appendix B). In the following analysis, we focus on the coherence of the propagation direction as opposed to the speed, because our estimates of sp_x and sp_y are somewhat sensitive to both data filtering and threshold, whereas the CCR location and propagation coherence are much more robust estimates. The coherence test is illustrated in Fig. 8b, where the green lines correspond to speed estimates based on subsamples of the CCR cross sections and the blue solid line represents the area-weighted mean speed. Figure 8c is similar to Fig. 8b, but for sp_y. In this example, $\mathrm{sp}_x = -23.4\,\mathrm{m\,s^{-1}}$, $\mathrm{sp}_y = 6.1\,\mathrm{m\,s^{-1}}$, $T_x = 1$, and $T_y = 1$, meaning that the CCR represents a region of enhanced cloudiness that moves northwestward coherently. The lifespan δt is given by the difference between the CCR initiation and end times and is 4 days for this example.

In the present analysis, we retain only CCRs that last for at least 1 day, span more than 500 km in latitude, and with centroids located between 120°E and 120°W and between 20°S and 20°N [we refer to this region as the tropical Pacific (TP)], which is the same area used for the EOF analysis in K16. The threshold is chosen to maximize the number of CCRs that last for more than 2 days and that span at least 1000 km meridionally. To calculate this optimized threshold, we detect CCRs at thresholds

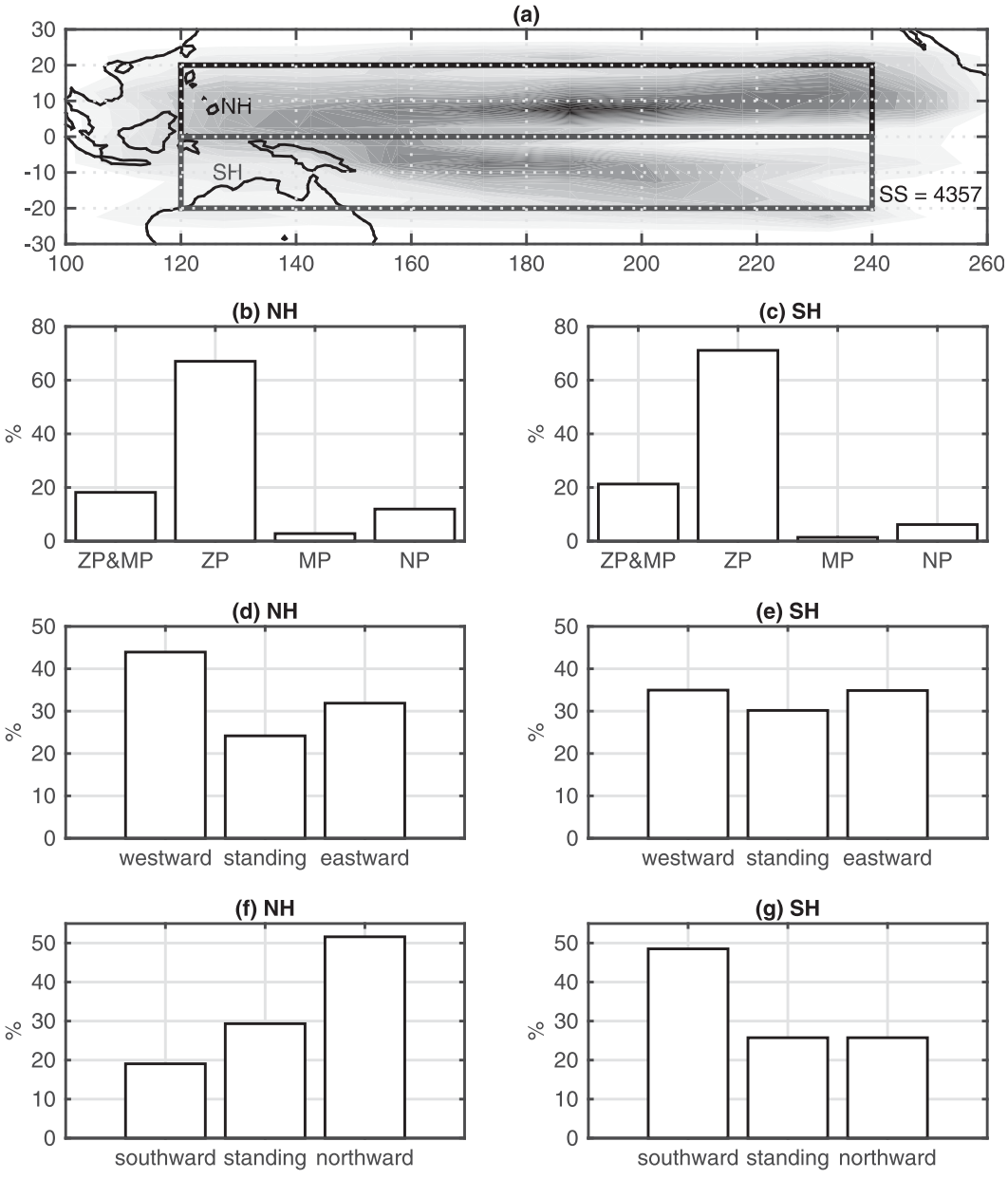

FIG. 9. (a) Longitude–latitude count of CCRs based on their centroids (L_x, L_y). (b) Partition of NTP CCRs among the ones that propagate coherently in both zonal and meridional directions (ZP&MP), only in the zonal direction (ZP), and only in the meridional direction (MP), as well as the ones that are not coherent (NP). (d) Partition of NTP CCRs that propagate coherently in the zonal direction among westward, standing, and eastward cases (details in the text). (f) Partition of NTP CCRs that propagate coherently in the meridional direction among southward, standing, and northward cases (details in the text). (c),(e),(g) As in (b),(d), and (f), respectively, but for STP CCRs.

ranging from the 1st to the 25th percentiles of the distribution of T_b^{10}, including data from all grid points in the TP region. To avoid a seasonal bias on the number of CCRs, the percentiles are calculated for December–February (DJF), March–May (MAM), June–August (JJA), and September–November (SON) independently. The optimum threshold varies between the 5th and 10th percentiles depending on the season, and since CCR location and coherence are not particularly sensitive to thresholds within this range, the results presented are based on the seasonal 5th percentile of T_b^{10}.

b. CCR statistics

Figure 9a shows a two-dimensional histogram of CCR centroids in the space of latitude and longitude ($L_x \times L_y$). Not surprisingly, the CCR distribution follows

the climatological South Pacific and intertropical convergence zones (SPCZ and ITCZ, respectively), with a primary peak in the Northern Hemisphere east of the date line and a secondary peak in the Southern Hemisphere around the date line. This distribution matches well with the regions of enhanced synoptic variability in Fig. 2c of K16. There are about 4300 CCRs that meet our size and location constraints, and because the region near the equator is relatively dry within the TP, CCRs are split into two disjoint sets: northern TP (NTP) if $L_y > 0$ and southern TP (STP) if $L_y < 0$. Figures 9b and 9c show that, based on our coherence criteria, and in both NTP and STP, about 60% of all CCRs are coherently propagating only zonally ($T_x = 1$ and $T_y = 0$), and about 20% are coherently propagating in the zonal and meridional directions ($T_x = 1$ and $T_y = 1$). Less than 5% of CCRs are coherent in only the meridional direction ($T_x = 0$ and $T_y = 1$), and between 5% and 10% of CCRs are not coherent in either direction ($T_x = 0$ and $T_y = 0$). While the propagation characteristics of CCRs are similar when seasons are analyzed independently, the $L_x \times L_y$ distribution varies substantially. The annual distribution (Fig. 9a) is in close agreement with the JJA and SON distributions (not shown), because about ⅔ of all CCRs occur in those seasons. During MAM there are two peaks in each hemisphere, one located to the west and the other to the east of the date line. In DJF the NH peak is largely shifted to the west. There is an additional peak at the northern edge of our domain in the eastern Pacific, which is likely due to extratropical intrusions (Kiladis 1998; Funatsu and Waugh 2008), and those are excluded from our analysis.

Figures 9d and 9e show the partition of the zonally coherent CCRs ($T_x = 1$) into westward ($\mathrm{sp}_x < -2.5\ \mathrm{m\ s^{-1}}$), eastward ($\mathrm{sp}_x > 2.5\ \mathrm{m\ s^{-1}}$), and standing ($|\mathrm{sp}_x| < 2.5\ \mathrm{m\ s^{-1}}$). The $2.5\ \mathrm{m\ s^{-1}}$ value is chosen based on the mean error in our estimate of sp_x and sp_y induced by changing CCR sizes by one grid point in each direction. Note that, while the zonal propagation partitioning is close to uniform in the STP, westward-moving CCRs are more dominant in the NTP. The partitioning for the annual mean shown in Figs. 9d and 9e does not have a strong seasonal cycle, except during SON, where westward-moving CCRs are even more dominant (about 50% of CCRs). This result is consistent with the results from Hendon and Liebmann (1991), as discussed in K16. Figures 9f and 9g show a similar partition, except for the meridionally coherent CCRs ($T_y = 1$). Based on Figs. 9f and 9g, CCRs in NTP tend to propagate northward, while CCRs in STP tend to propagate southward, which is consistent with the lag-regression analysis from K16. We also note that there is no strong seasonal cycle in the distributions displayed in Figs. 9f and 9g (not shown).

Aside from the similar propagation characteristics between CCRs in the STP and NTP, these two sets are also similar in lifespan and size (not shown). In addition, for about 80% of NTP CCRs, there is at least one STP CCR that occurs less than 3 days apart from that NTP CCR, where the timing is based on the difference between the two L_t periods. This result is also in agreement with the EOF and spectral analysis from K16 in that it suggests a link between CCRs in each hemisphere. In the next section, we turn to a composite analysis of CCRs that further supports this relationship.

c. CCR composites

Composites are calculated by shifting L_x to a center longitude and L_t to day 0. Statistical significance of the composite is then estimated using a t test at each grid point. This calculation was done using 2–20-day bandpass-filtered T_b at the original 0.5° spatial resolution and ERAI data at 2.5° to characterize dynamical anomalies associated with the CCRs. To identify MRG versus EIG types of disturbances, the results shown next include only CCRs that are zonally coherent and with centroids in the NTP. The shaded and contoured regions in the lag composites (Figs. 10 and 11) indicate regions where the anomalies are statistically significant and larger than one standard deviation. In addition, 2–20-day-filtered winds at 850 hPa are shown.

Figure 10 compares the lag–longitude composites of NTP CCRs, based on the partitioning shown in Fig. 9d. By construction, the anomalous T_b patterns indicate westward, standing, and eastward propagation from top to bottom, respectively. In the case of the westward composite (Fig. 10a), meridional wind anomalies are roughly out of phase with T_b, which is consistent with the MRG theoretical structure. This relationship is weaker in the standing composite (Fig. 10b), where, in addition, the meridional winds and T_b coupling last for a much shorter period than indicated in the westward case (Fig. 10a). In contrast to the westward and standing cases, the eastward CCR meridional wind pattern is not strongly coupled to T_b (Fig. 10e). We note that the zonal wind composites show the inverse behavior: zonal wind anomalies are nearly standing in the westward case (Fig. 10b), they suggest eastward propagation in the standing case (Fig. 10d), and they are strongly coupled with the eastward-moving T_b anomalies in the eastward case (Fig. 10f). In addition, as expected from EIG theory, assuming that T_b is in phase with low-level convergence, Fig. 10f also shows T_b and zonal wind anomalies nearly in quadrature. The estimated

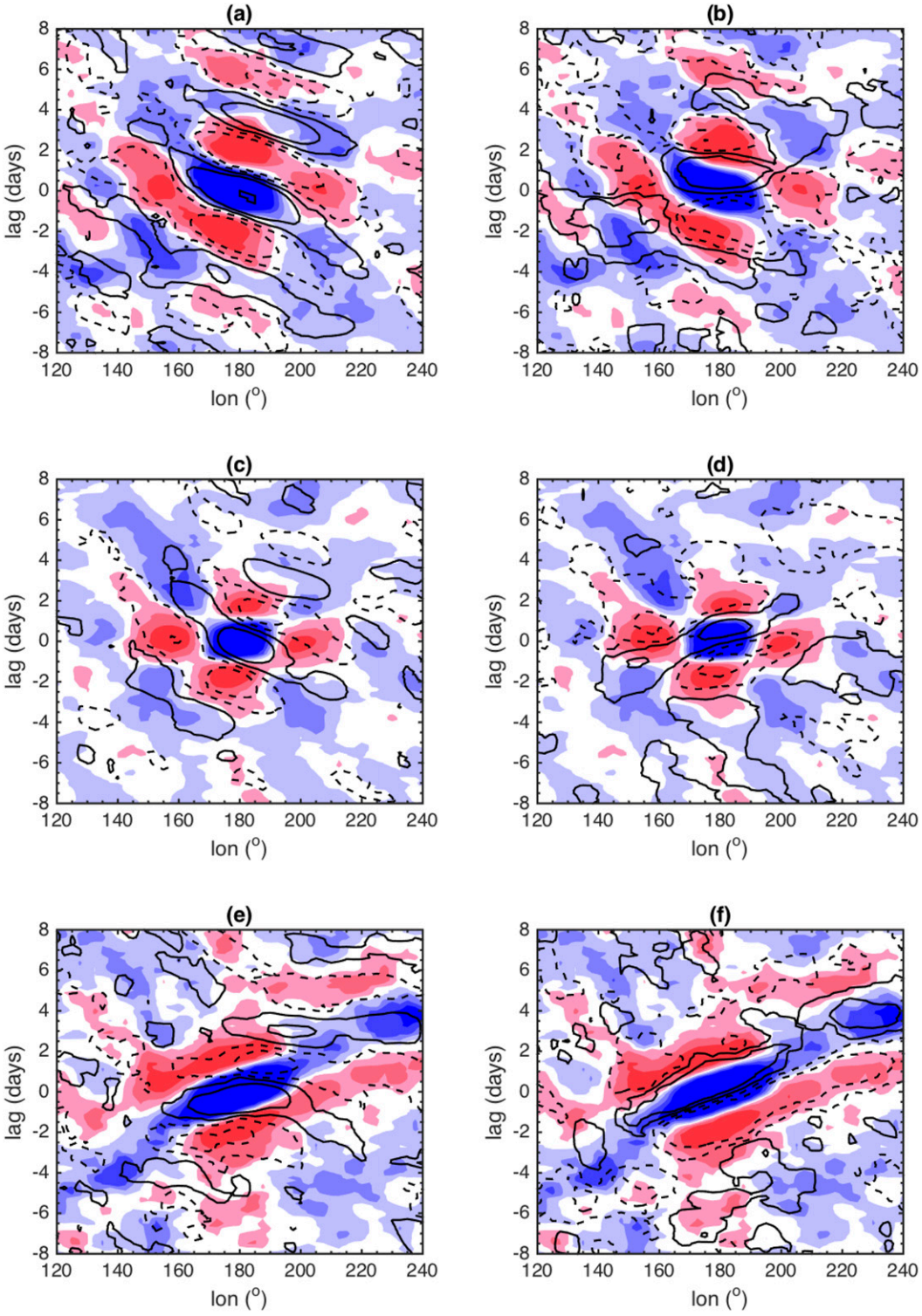

FIG. 10. (a) Lag–longitude NTP westward CCR composites of 2–20-day T_b (shading) averaged from 2.5° to 12.5°N and 2–20-day meridional winds at 850 hPa (contours) averaged from 7.5°S to 7.5°N. (b) As in (a), but for zonal winds at 850 hPa averaged from 2.5° to 12.5°N. (c),(d) As in (a) and (b), respectively, but for NTP standing CCR composites. (e),(f) As in (a) and (b), respectively, but for NTP eastward CCR composites. Shading interval is 1 K, starting at +1 (red) and −1 K (blue). Contour interval is 0.2 m s^{-1}, starting at +0.1 (solid) and −0.1 m s^{-1} (dashed).

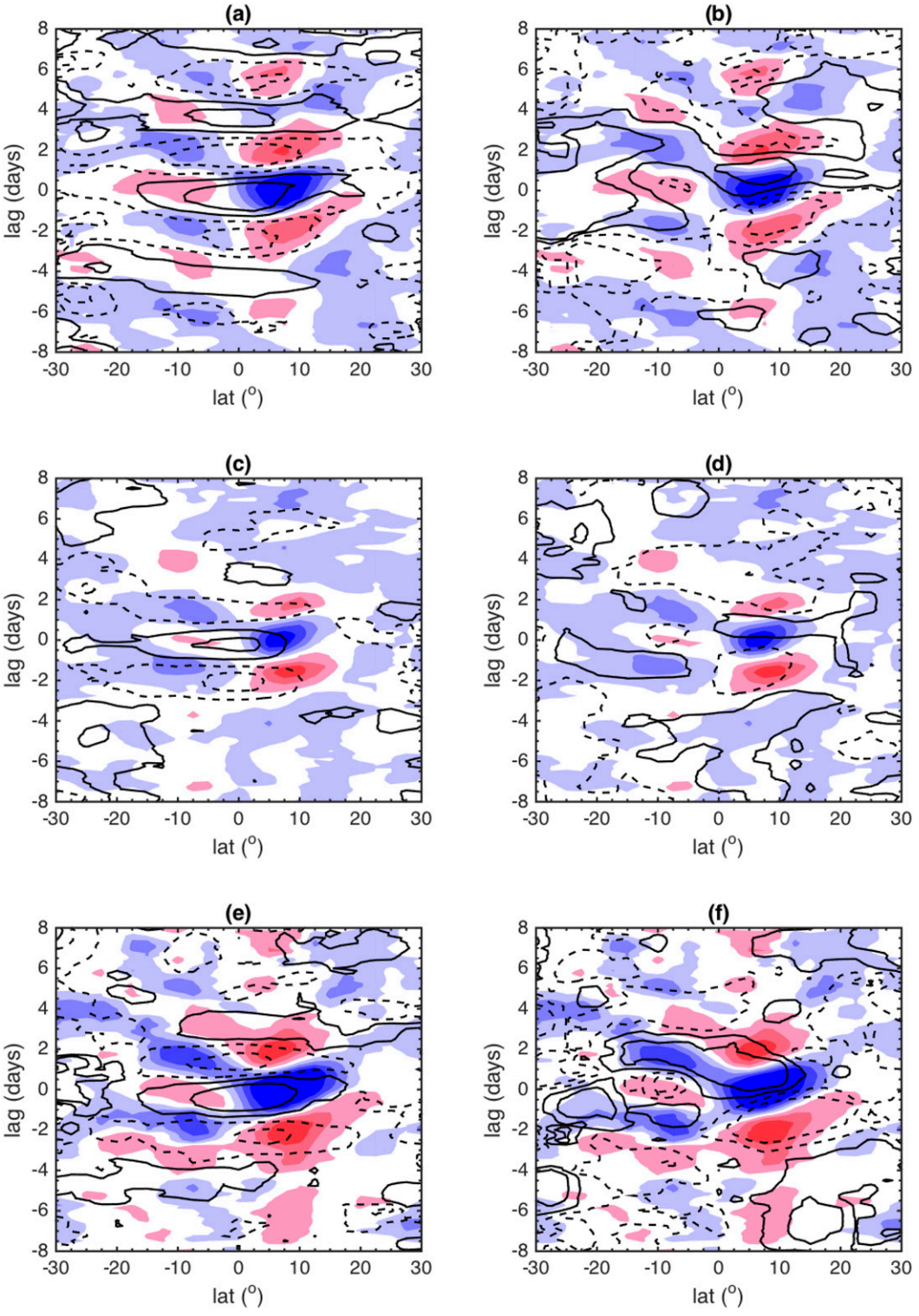

FIG. 11. As in Fig. 10, but for lag–latitude NTP CCR composites. In all panels, the zonal average is calculated from 160°E to 160°W. Shading and contours also as in Fig. 10.

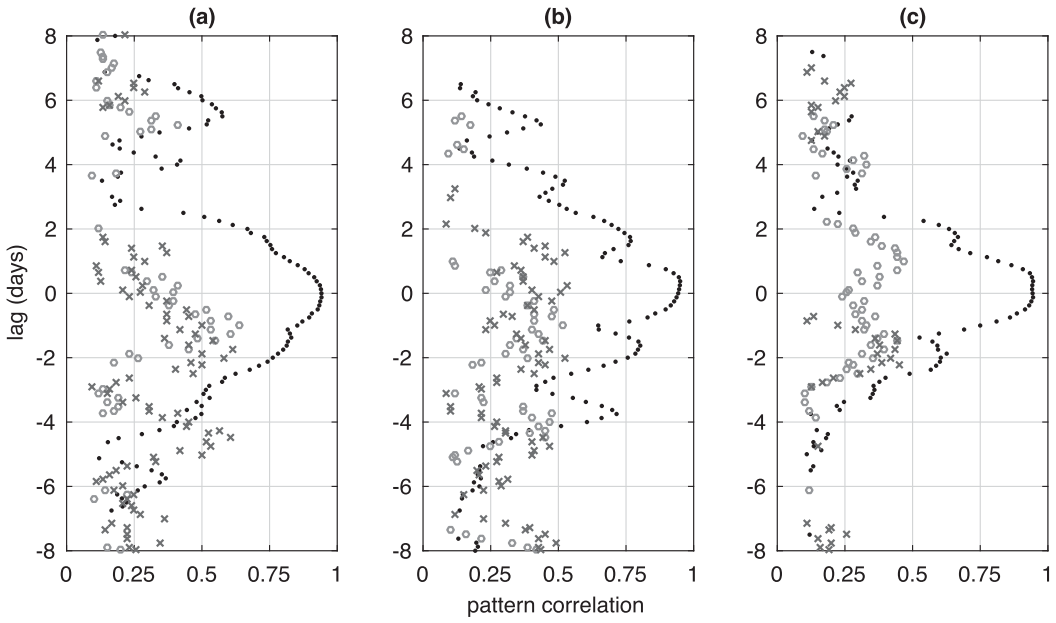

FIG. 12. Lag–pattern correlations between NTP and STP CCR composites for T_b (black dots), meridional wind at 850 hPa (gray crosses), and zonal wind at 850 hPa (gray circles) for (a) westward-moving, (b) standing, and (c) eastward-moving CCRs. Only statistically significant correlations are shown (details in the text).

phase speed based on the slope of T_b anomalies is around $20\,\mathrm{m\,s^{-1}}$ for westward-moving CCRs and $25\,\mathrm{m\,s^{-1}}$ for the eastward ones.

Figure 11 is similar to Fig. 10, but for lag–latitude composites. In the three cases, T_b anomalies are nearly antisymmetric with respect to the equator, and meridional wind anomalies are nearly symmetric, features both in agreement with the expected MRG/EIG structure. Interestingly, poleward T_b propagation is also evident in all three cases. One notable difference among the three composites is that Fig. 11b suggests that the standing cases have shorter periods than both eastward and westward cases. Specifically, the periods inferred from the meridional wind composites at the equator are 4.3 days for westward cases, 3.4 days for standing cases, and 3.9 days for eastward cases. In addition, as in Fig. 10, the meridional wind–T_b coupling persists the longest for the westward composite (Fig. 11a). Zonal wind anomalies (right column in Fig. 11) are relatively less organized, but there is some suggestion of antisymmetry, particularly in the eastward composite (Fig. 11f). Figure 11 also indicates that poleward propagation inferred from both meridional and zonal wind anomalies is much weaker than for T_b anomalies. While Matsuno's theory predicts antisymmetric divergence patterns for MRGs and EIGs, the asymmetry with respect to the equator in the T_b composites is evident in all cases, and there are a number of reasons for that to occur. For instance, not all CCRs represent an MRG or EIG type of disturbance; therefore, while there is always a negative T_b perturbation north of the equator, there is not necessarily a corresponding positive T_b anomaly south of the equator for every composite member. Another potential source of asymmetry comes from the fact that convection associated with each CCR is likely not entirely explained by low-level convergence associated with MRGs or EIGs. For example, an antisymmetric disturbance could be a response to off-equatorial heating, in which case the CCR would include T_b anomalies from both the forcing and response. Other sources, such as nonlinearities and the basic state, are discussed in section 5.

The relationship between STP and NTP CCRs is quantified by calculating the pattern correlation between the composites at each lag using only NTP versus only STP CCRs. The pattern correlation for all variables is calculated after flipping north and south grid points and switching the sign of the meridional wind of the STP composites, which means that, when NTP and STP composites are similar, the pattern correlation should be positive. Focusing once more only on zonally coherent CCRs and the associated circulation at 850 hPa, Fig. 12 shows the pattern correlation of NTP and STP T_b, meridional wind, and zonal wind anomalies for westward, standing, and eastward CCRs. Only correlations that are significant at the 95% confidence level are shown, where it is assumed that anomalies follow a normal distribution. Also, only grid points where both NTP and STP

anomalies are significant are used to calculate each lag's pattern correlation. Note that, in all panels, the strongest correlations occur between NTP and STP T_b anomalies, followed by meridional wind anomalies for the westward (Fig. 12a) and standing (Fig. 12b) composites, and zonal wind anomalies for the eastward composite (Fig. 12c). As expected, the pattern correlation decays away from lag 0 in all cases and for all variables. Interestingly, while significant correlations persist the least in the case of the standing composites, in this case, T_b pattern correlations above 0.5 last the longest (Fig. 12b). Overall, Fig. 12 shows that NTP and STP CCR composites are in reasonable agreement with one another, particularly during the 2–3 days on either side of lag 0. Importantly, the object-approach results reported here using T_b^{10} are very similar to those when using T_{b26} (not shown). Moreover, we obtain periods consistent with the spectral and EOF analysis of K16, despite the fact that no bandpass temporal filtering was applied to T_b in order to generate the original CCR dataset.

Based on the composites shown in Figs. 10 and 11, we conclude that westward and eastward CCRs are in reasonable agreement with the expected behavior of MRGs and IGs from Matsuno's theory. In view of the theoretical structures of these modes shown in section 2, perhaps these results are not too surprising. In a shallow-water system, both MRGs and EIGs can be excited by off-equatorial disturbances (Silva Dias et al. 1983; Zhang and Webster 1992; Zhang 1993). Because the theoretical MRG divergence is dominated by its meridional component, assuming that westward-moving CCRs are representing convection associated with MRG-like disturbances, we would expect to see a stronger relationship between T_b and meridional divergence as a result of north–south wind anomalies. This is in contrast to the theoretical divergence for EIGs that, for large enough zonal wavenumbers, is dominated by its zonal component; thus, EIG T_b and zonal wind anomalies should be more strongly related, which is what the eastward CCR composites suggest. Another remarkable feature of the composites is that the standing CCR composites show westward-moving meridional wind anomalies and eastward-moving zonal wind anomalies. This result suggests that standing CCRs are indeed cases of simultaneous linear interference between MRG and EIG types of disturbances, because in this case T_b anomalies would be coupled with the meridional winds associated with the westward-moving disturbance, while the zonal wind would be associated with the eastward-moving disturbance. Specifically, our interpretation of Figs. 10c and 10d is based on the following approximations:

$$T_b \propto -\mathrm{div}_{\mathrm{EIG}} \propto -\partial_x u_{\mathrm{EIG}}, \tag{10}$$

$$T_b \propto -\mathrm{div}_{\mathrm{MRG}} \propto -\partial_y v_{\mathrm{MRG}}. \tag{11}$$

Note that, because this is an approximation based on the dominant component of the divergence, our interference interpretation is not inconsistent with section 2, where it is shown that, for the MRG and EIG divergences to match the total, MRG circulation has to be stronger than the EIG circulation.

5. Summary and conclusions

Results from two completely independent analyses, one based on EOFs and the other one based on object tracking, are used to characterize the behavior of synoptic-scale convective activity in the tropical central Pacific. The EOF analysis is based on the results from K16, and the object-based algorithm involves detecting contiguous regions of enhanced cloudiness in the space of longitude, latitude, and time, referred to as CCRs. To motivate the latter approach, we first calculate EOFs of idealized data consisting of only MRG and EIG theoretical modes. This preliminary analysis reveals commonalities with the observational results from the EOF decomposition of K16. In particular, it indicates that alternating or overlapping patterns of westward and eastward disturbances are hardly distinguishable from one another based on the EOF approach. This result motivates the hypothesis that the standing pattern of oscillation in the tropical central Pacific discussed in K16 is due to an interference between MRG- and EIG-like disturbances. To further investigate this hypothesis, we then apply an independent analysis based on the object-based algorithm mentioned above. In agreement with the antisymmetric component of the space–time power spectrum of T_b (K16, their Fig. 1a) that shows enhanced power along the dispersion curves of the MRG and EIG modes of Matsuno's theory, the object-based algorithm identifies a large percentage of CCRs that are zonally coherent. Depending on whether CCRs are located north or south of the equator, roughly 25%–30% of the zonally coherent CCRs are standing, 35%–45% are westward propagating, and 30%–35% are eastward propagating (see Figs. 9d and 9e). These results support the interpretation that the EOF patterns from K16 are mostly due to an alternating interference between westward and eastward synoptic disturbances.

The CCR composites revealed that these synoptic disturbances follow theoretical linear dynamics to a remarkable degree. For instance, consistent with K16 and with theoretical MRGs, the westward-moving CCRs are associated with T_b and low-level meridional wind anomalies moving coherently at about 21 m s^{-1} toward

the west with a period of about 4.25 days. Also, as predicted by MRG theory, T_b anomalies are antisymmetric with respect to the equator, whereas meridional wind anomalies are symmetric. The zonal wind, however, is much less organized, which is not surprising, because the MRG meridional divergence controls the sign of the total divergence (as shown in section 2), implying that the association between cloudiness and the zonal wind flow would be much harder to detect in the composites than the meridional flow component. Analogous reasoning supports the more noisy meridional flow in comparison with the zonal flow associated with eastward-moving CCRs because EIG divergence is dominated by its zonal component. Note that, because it is the low-level divergence that is related to T_b and not the winds, the composites in Figs. 10 and 11 cannot capture the theoretical prediction that the MRG winds have to be stronger than the EIG winds in order for their divergences to have the same amplitude.

The structure of eastward-moving CCRs is also in agreement with EIGs from shallow-water theory in that their T_b and zonal wind anomalies are antisymmetric with respect to the equator, whereas meridional wind anomalies are symmetric. Moreover, as estimated by K16, the eastward-moving CCRs propagate at about 25 m s^{-1}, and their period is about 3.5 days. The zonally standing composites are particularly interesting as they show low-level zonal winds moving toward the east, which is likely characterizing the EIG component of an "MRG+EIG"-like interference signal, along with meridional winds propagating to the west consistent with the MRG component of this interference. Our results, therefore, imply that 25%–30% of standing CCRs are cases of a simultaneous interference signal that is also consistent with shallow-water theory in that they behave similarly to our idealized MRG+EIG test case.

While the analyses presented here in combination with K16 provide substantial observational evidence of the expected contrast in behavior between MRGs and EIGs from shallow-water theory, there are also notable differences. For example, the observed disturbances often deviate from Matsuno's symmetric or antisymmetric amplitudes with respect to the equator, and this could be due to a variety of processes. For instance, at times there is likely to be interference with other types of equatorial waves, such as Kelvin, equatorial Rossby, or easterly waves. Another potential impact to the behavior of the waves involves horizontal and vertical wind shear within the basic state, which is known to affect the eigenfunctions of the shallow-water system (Zhang and Webster 1989, 1992; Zhang 1993; Han and Khouider 2010; Monteiro et al. 2014). In addition, nonlinear effects coming from moisture–wave coupling may play a substantial role in altering the disturbance structures. Another important distinction from linear theory is related to the poleward propagation of T_b anomalies that both the object approach and EOF analysis imply. This meridional propagation could, for example, be due to a secondary meridional circulation induced by latent heating associated with the MRG- and EIG-like disturbances. As discussed by K16, we plan to further investigate these departures from MRG and EIG linear dynamics through an analysis of MRG and EIG moisture budgets in a future study.

Acknowledgments. We thank Brant Liebmann, Takeshi Horinouchi, and two anonymous reviewers for thoughtful and insightful comments on an original draft of this paper and Maria Gehne for guidance on several aspects of the analysis techniques used here.

APPENDIX A

MRG and EIG Interference Signal with Noise

A remarkable difference between the EOF analysis of shallow-water modes and observed data is the amount of variance explained by the leading patterns. Specifically, K16 show that the first two EOF components of T_{b26} explain about 6.5% of the total variance, in contrast with the idealized cases from section 3 that explain about 99%. This is likely because the T_{b26} dataset is made up of organized convective variability at multiple interacting scales, as well as background noise. Variance-based methods are known to be very sensitive to noise (North et al. 1982), which is easily illustrated by adding red noise to the "MRG+EIG" dataset:

$$\mathrm{div}_r = \mathrm{div}_{\mathrm{MRG+EIG}} + r. \tag{A1}$$

The noise r is modeled using a univariate lag-1 autoregressive process:

$$r^n(x,y) = \alpha r^{n-1}(x,y) + z_n(x,y), \tag{A2}$$

where n is the discrete time step, α is the assumed lag-1 autocorrelation, and z_n is taken from Gaussian white noise (Torrence and Compo 1998). Assuming a decorrelation time of 2 days, and normalizing r so that its amplitude is at most 10% of the wave amplitude, the leading EOFs and PCs of div_r are in close agreement with the ones from $\mathrm{div}_{\mathrm{MRG+EIG}}$ (not shown). On the other hand, noise has a substantial impact on the amount of explained variance, which, for this particular choice of parameters, decreases to about 60%. In the case of white noise ($\alpha = 0$), the leading EOFs are still similar to the

case without noise but explain only 24% of the total variance.

While a complete analysis of the impact of various types of noise in the EOF decomposition is beyond the scope of this paper, the examples shown here suggest that the relative low amount of variance explained may be due to noise and/or multiscale convective processes not necessarily related to MRGs and EIGs.

APPENDIX B

The Propagation Coherence Criteria

CCRs are connected regions such that $T_b(x, y, t) \leq T_{b0}$, where Tb_0 is the threshold temperature. Mathematically, they are represented by

$$\mathrm{CCR}(x,y,t) = 1 \quad \text{if} \quad T_b(x,y,t) \leq T_{b0} \quad \text{and} \tag{B1}$$

$$\mathrm{CCR}(x,y,t) = 0 \quad \text{if} \quad T_b(x,y,t) > T_{b0}, \tag{B2}$$

where (x, y) are the zonal and meridional distances and t is time. The mean CCR in the meridional and zonal directions are defined as $\overline{\mathrm{CCR}(x,t)}^{y}$ and $\overline{\mathrm{CCR}(y,t)}^{x}$. The phase speeds sp_x and sp_y are then calculated by applying a Radon transform to $\overline{\mathrm{CCR}(x,t)}^{y}$ and $\overline{\mathrm{CCR}(y,t)}^{x}$, respectively [as illustrated in Fig. B1 in Dias et al. (2012)]. The only differences in the methodology used here are that we calculate an area-weighted average, and we do not use a variance cutoff, which means that every CCR has an assigned phase speed estimate. This step is illustrated in the case of the CCR shown in Fig. 8a, where sp_x and sp_y correspond to the solid lines in Figs. 8b and 8c. To test for coherence of the CCR propagation speeds, we apply a bootstrap method where we create, for each CCR, 1000 samples of random sets of cross sections to calculate the zonal or the meridional CCR average and then estimate sp_x^r and sp_y^r for each realization of this process. The dotted green lines in Figs. 8b and 8c represent realizations of the phase speed estimates. Intuitively, we are testing whether the CCR speeds inferred from its mean is representative of the CCR propagation direction through its lifetime. The samples of sp_x^r and sp_y^r yield an estimate for the confidence interval of sp_x and sp_y. With that, we define zonal (meridional) coherence when sp_x (sp_y) lies within the 90% confidence interval, with the CCR considered not zonally (meridionally) coherent otherwise.

REFERENCES

Dias, J., and G. N. Kiladis, 2014: Influence of the basic state zonal flow on convectively coupled equatorial waves. *Geophys. Res. Lett.*, **41**, 6904–6913, doi:10.1002/2014GL061476.

——, S. N. Tulich, and G. N. Kiladis, 2012: An object-based approach to assessing tropical convection organization. *J. Atmos. Sci.*, **69**, 2488–2504, doi:10.1175/JAS-D-11-0293.1

Frank, W. M., and P. E. Roundy, 2006: The role of tropical waves in tropical cyclogenesis. *Mon. Wea. Rev.*, **134**, 2397–2417, doi:10.1175/MWR3204.1

Frierson, D. M. W., D. Kim, I.-S. Kang, M.-I. Lee, and J. Lin, 2011: Structure of AGCM-simulated convectively coupled Kelvin waves and sensitivity to convective parameterization. *J. Atmos. Sci.*, **68**, 26–45, doi:10.1175/2010JAS3356.1

Funatsu, B. M., and D. W. Waugh, 2008: Connections between potential vorticity intrusions and convection in the eastern tropical Pacific. *J. Atmos. Sci.*, **65**, 987–1002, doi:10.1175/2007JAS2248.1.

Gloeckler, L. C., and P. E. Roundy, 2013: Modulation of the extratropical circulation by combined activity of the Madden–Julian oscillation and equatorial Rossby waves during boreal winter. *Mon. Wea. Rev.*, **141**, 1347–1357, doi:10.1175/MWR-D-12-00179.1.

Goswami, P., and B. N. Goswami, 1991: Modification of n = 0 equatorial waves due to interaction between convection and dynamics. *J. Atmos. Sci.*, **48**, 2231–2244, doi:10.1175/1520-0469(1991)048⟨2231:MOEWDT⟩2.0.CO;2.

Han, Y., and B. Khouider, 2010: Convectively coupled waves in a sheared environment. *J. Atmos. Sci.*, **67**, 2913–2942, doi:10.1175/2010JAS3335.1.

Hayashi, Y., 1976: Non-singular resonance of equatorial waves under the radiation condition. *J. Atmos. Sci.*, **33**, 183–201, doi:10.1175/1520-0469(1976)033⟨0183:NSROEW⟩2.0.CO;2.

Hendon, H. H., and B. Liebmann, 1991: The structure and annual variation of antisymmetric fluctuations of tropical convection and their association with Rossby–gravity waves. *J. Atmos. Sci.*, **48**, 2127–2140, doi:10.1175/1520-0469(1991)048<2127:TSAAVO>2.0.CO;2

Hung, M.-P., J.-L. Lin, W. Wang, D. Kim, T. Shinoda, and S. J. Weaver, 2013: MJO and convectively coupled equatorial waves simulated by CMIP5 climate models. *J. Climate*, **26**, 6185–6214, doi:10.1175/JCLI-D-12-00541.1.

Itoh, H., and M. Ghil, 1988: The generation mechanism of mixed Rossby–gravity waves in the equatorial troposphere. *J. Atmos. Sci.*, **45**, 585–604, doi:10.1175/1520-0469(1988)045⟨0585:TGMOMR⟩2.0.CO;2.

Kiladis, G. N., 1998: Observations of Rossby waves linked to convection over the eastern tropical Pacific. *J. Atmos. Sci.*, **55**, 321–339, doi:10.1175/1520-0469(1998)055⟨0321:OORWLT⟩2.0.CO;2.

——, M. C. Wheeler, P. T. Haertel, K. H. Straub, and P. E. Roundy, 2009: Convectively coupled equatorial waves. *Rev. Geophys.*, **47**, 374–399, doi:10.1175/1520-0469(1999)056<0374:CCEWAO>2.0.CO;2.

——, J. Dias, and M. Gehne, 2016: The relationship between equatorial mixed Rossby–gravity and eastward inertio-gravity waves. Part I. *J. Atmos. Sci.*, **73**, 2123–2145, doi:10.1175/JAS-D-15-0230.1.

Lamb, V. R., 1973: The response of a tropical atmosphere to middle latitude forcing. Ph.D. thesis, University of California, Los Angeles, 151 pp.

Liebmann, B., and H. H. Hendon, 1990: Synoptic-scale disturbances near the equator. *J. Atmos. Sci.*, **47**, 1463–1479, doi:10.1175/1520-0469(1990)047<1463:SSDNTE>2.0.CO;2

Lin, J. L., M. I. Lee, D. Kim, I. S. Kang, and D. M. W. Frierson, 2008: The impacts of convective parameterization and moisture triggering on AGCM-simulated convectively coupled equatorial waves. *J. Climate*, **21**, 883–909, doi:10.1175/2007JCLI1790.1.

Magaña, V., and M. Yanai, 1995: Mixed Rossby–gravity waves triggered by lateral forcing. *J. Atmos. Sci.*, **52**, 1473–1486, doi:10.1175/1520-0469(1995)052<1473:MRWTBL>2.0.CO;2

Mak, M.-K., 1969: Laterally driven stochastic motions in the tropics. *J. Atmos. Sci.*, **26**, 41–64, doi:10.1175/1520-0469(1969)026<0041:LDSMIT>2.0.CO;2

Matsuno, T., 1966: Quasi-geostrophic motions in the equatorial area. *J. Meteor. Soc. Japan*, **44**, 25–43.

Monteiro, J. M., A. F. Adams, J. M. Wallace, and J. S. Sukhatme, 2014: Interpreting the upper level structure of the Madden–Julian oscillation. *Geophys. Res. Lett.*, **41**, 9158–9165, doi:10.1002/2014GL062518.

North, G. R., T. L. Bell, R. F. Cahalan, and F. J. Moeng, 1982: Sampling errors in the estimation of empirical orthogonal functions. *Mon. Wea. Rev.*, **110**, 699–706, doi:10.1175/1520-0493(1982)110<0699:SEITEO>2.0.CO;2

Raupp, C. F. M., and P. L. Silva Dias, 2005: Excitation mechanism of mixed Rossby–gravity waves in the equatorial atmosphere: Role of the nonlinear interactions among equatorial waves. *J. Atmos. Sci.*, **62**, 1446–1462, doi:10.1175/JAS3412.1

Schreck, C. J., J. Molinari, and K. I. Mohr, 2011: Attributing tropical cyclogenesis to equatorial waves in the western north Pacific. *J. Atmos. Sci.*, **68**, 195–209, doi:10.1175/2010JAS3396.1

Silva Dias, P. L., W. H. Schubert, and M. DeMaria, 1983: Large-scale response of the tropical atmosphere to transient convection. *J. Atmos. Sci.*, **40**, 2689–2707, doi:10.1175/1520-0469(1983)040<2689:LSROTT>2.0.CO;2

Straub, K. H., P. T. Haertel, and G. N. Kiladis, 2010: An analysis of convectively coupled Kelvin waves in 20 WCRP CMIP3 global coupled climate models. *J. Climate*, **23**, 3031–3056, doi:10.1175/2009JCLI3422.1

Torrence, C., and G. P. Compo, 1998: A practical guide to wavelet analysis. *Bull. Amer. Meteor. Soc.*, **79**, 61–78, doi:10.1175/1520-0477(1998)079<0061:APGTWA>2.0.CO;2

Wallace, J. M., and C. P. Chang, 1969: Spectrum analysis of large-scale wave disturbances in the tropical lower troposphere. *J. Atmos. Sci.*, **26**, 1010–1025, doi:10.1175/1520-0469(1969)026<1010:SAOLSW>2.0.CO;2

Wang, B., and X. Xie, 1996: Low-frequency equatorial waves in vertically sheared zonal flow. Part I: Stable waves. *J. Atmos. Sci.*, **53**, 3424–3437, doi:10.1175/1520-0469(1996)053<0449:LFEWIV>2.0.CO;2.

Wheeler, M. C., and G. N. Kiladis, 1999: Convectively coupled equatorial waves: Analysis of clouds and temperature in the wavenumber–frequency domain. *J. Atmos. Sci.*, **56**, 374–399, doi:10.1175/1520-0469(1999)056<0374:CCEWAO>2.0.CO;2

——, ——, and P. J. Webster, 2000: Large-scale dynamical fields associated with convectively coupled equatorial waves. *J. Atmos. Sci.*, **57**, 613–640, doi:10.1175/1520-0469(2000)057<0613:LSDFAW>2.0.CO;2

Wilson, J. D., and M. Mak, 1984: Tropical response to lateral forcing with a latitudinally and zonally nonuniform basic state. *J. Atmos. Sci.*, **41**, 1187–1201, doi:10.1175/1520-0469(1984)041<1187:TRTLFW>2.0.CO;2

Xie, X., and B. Wang, 1996: Low-frequency equatorial waves in vertically sheared zonal flow. Part II: Unstable waves. *J. Atmos. Sci.*, **53**, 3589–3605, doi:10.1175/1520-0469(1996)053<3589:LFEWIV>2.0.CO;2

Yanai, M., and M.-M. Lu, 1983: Equatorially trapped waves at the 200 mb level and their association with meridional convergence of wave energy flux. *J. Atmos. Sci.*, **40**, 2785–2803, doi:10.1175/1520-0469(1983)040<2785:ETWATM>2.0.CO;2

——, T. Maruyama, T. Nitta, and Y. Hayashi, 1968: Power spectra of large-scale disturbances over the tropical Pacific. *J. Meteor. Soc. Japan*, **46**, 291–294.

Zangvil, A., and M. Yanai, 1980: Upper tropospheric waves in the tropics. Part I: Dynamical analysis in the wavenumber-frequency domain. *J. Atmos. Sci.*, **37**, 283–298, doi:10.1175/1520-0469(1980)037<0283:UTWITT>2.0.CO;2

Zhang, C., 1993: Laterally forced equatorial perturbations in a linear model. Part II: Mobile forcing. *J. Atmos. Sci.*, **50**, 807–821, doi:10.1175/1520-0469(1993)050<0807:LFEPIA>2.0.CO;2

——, and P. J. Webster, 1989: Effects of zonal flows on equatorially trapped waves. *J. Atmos. Sci.*, **46**, 3632–3652, doi:10.1175/1520-0469(1989)046<3632:EOZFOE>2.0.CO;2

——, and ——, 1992: Laterally forced equatorial perturbations in a linear model. Part I: Stationary transient forcing. *J. Atmos. Sci.*, **49**, 585–607, doi:10.1175/1520-0469(1992)049<0585:LFEPIA>2.0.CO;2

Zhou, L., and I.-S. Kang, 2013: Influence of convective momentum transport on mixed Rossby–gravity waves: A contribution to tropical 2-day waves. *J. Atmos. Sci.*, **70**, 2467–2475, doi:10.1175/JAS-D-12-0300.1